Editors' Suggestion

Multiscale time-dependent density functional theory for a unified description of ultrafast dynamics: Pulsed light, electron, and lattice motions in crystalline solids

Atsushi Yamada* and Kazuhiro Yabana
Center for Computational Sciences, University of Tsukuba, 1-1-1 Tennodai, Tsukuba, Ibaraki 305-8577, Japan

(Received 17 October 2018; revised manuscript received 21 April 2019; published 3 June 2019)

We have developed a multiscale computational scheme to describe coupled nonlinear dynamics of light electromagnetic field, electrons, and lattice motions in crystalline solids, where first-principles molecular dynamics based on time-dependent density-functional theory is used to describe the microscopic dynamics. The method is applicable to wide phenomena in nonlinear and ultrafast optics. To show usefulness of the method, we apply it to a pump-probe measurement of coherent phonon in diamond where a stimulated Raman wave is generated and amplified during the propagation of the probe pulse.

DOI: 10.1103/PhysRevB.99.245103

I. INTRODUCTION

Nonlinear optics in solids is the study of the interaction of intense laser light with bulk materials [1–3]. It is intrinsically a complex phenomena arising from coupled nonlinear dynamics of light electromagnetic fields, electrons, and lattice motions. They are characterized by two different spatial scales, micrometer for the wavelength of the light and less than nanometer for the dynamics of electrons and ions.

In early development, nonlinear optics has developed mainly in perturbative regime and in frequency domain [4,5]. However, it has changed rapidly and drastically. Nowadays, measurements are carried out quite often in time domains using a pump-probe technique as a typical method and the time resolution reaches a few tens of attoseconds [6,7]. Extremely nonlinear phenomena have attracted interest such as high harmonic generation in solids [8,9], ultrafast control of electron motion in dielectrics that aims for future signal processing using pulsed light [10–12], ultrafast coherent optical phonon control [13–22], and photoinduced structural phase transition of materials [23–26].

We report in this paper progress to develop a first-principles computational method to describe nonlinear optical processes in solids that arise from coupled dynamics of light electromagnetic fields, electrons, and lattice motions in crystalline solids. In condensed matter physics and materials sciences, first-principles computational approaches represented by density-functional theory have been widely used to describe electronic structures and recognized as an indispensable tool [27]. Development of first-principles approaches in optical sciences is, however, still in a premature stage due to the complexity of the phenomena and the requirement of describing time-dependent dynamics.

Our method utilizes time-dependent density-functional theory (TDDFT) for microscopic dynamics of electrons [28,29]. The TDDFT is an extension of the density-functional theory so as to be applicable to electron dynamics in real time [30]. In the microscopic scale, ultrafast dynamics of electrons have been successfully explored solving the time-dependent Kohn-Sham (TDKS) equation, the basic equation of TDDFT, in real time under light electric fields [31–33].

We have further developed a multiscale scheme to describe a propagation of strong light electromagnetic fields in bulk media [34]. Here the Maxwell equations are solved to describe the macroscopic light propagation while the TDKS equation is solved to describe the microscopic electron dynamics in unit cells of solids. The method can faithfully mimic experimental setups simulating pump-probe measurements. It has been applied to investigate extremely nonlinear optical processes in dielectrics using few-cycle femto- and attosecond pulses [11,12].

In the present paper, we extend the multiscale approach to incorporate lattice dynamics, combining a first-principles Ehrenfest molecular dynamics (MD) approach [35]. The extended approach, namely Maxwell + TDDFT + MD multiscale simulation, will be capable of describing vast nonlinear optical phenomena involving lattice dynamics such as stimulated Raman scattering [1–3]. We will later show a simulation of the impulsively stimulated Raman scattering (ISRS) spectroscopy as the first application of the method, where the pump pulse generates coherent optical phonon over the medium and the succeeding probe pulse interacts with the coherent phonon to produce the transmission wave signals that include the generation and the amplification of the stimulated Raman scattering wave.

The organization of this paper is as follows. In Sec. II, we present our formalism of the extended multiscale method. In Sec. III, a system to demonstrate our method and numerical details are explained. Results of the simulation of the pump-probe measurement for coherent phonon are shown in Sec. IV. In Sec. V, a summary will be presented.

II. FORMALISM

In the present paper, we develop a formalism to describe a propagation of light electromagnetic fields in a medium starting with the first-principles, microscopic calculations of

*ayamada@ccs.tsukuba.ac.jp

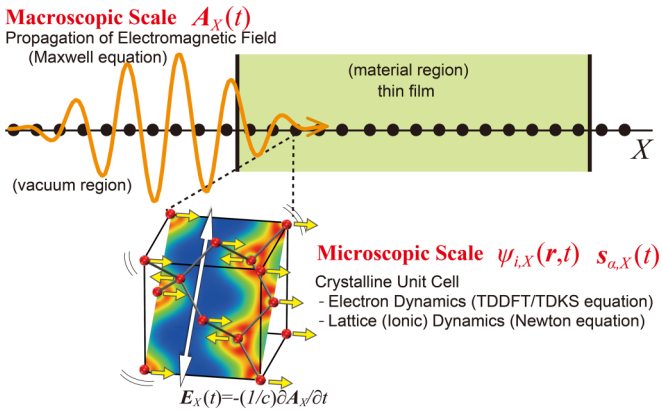

FIG. 1. Schematic illustration of the multiscale scheme for a one-dimensional light propagation through a thin-film medium. The macroscopic spacial coordinate is expressed by X.

electronic and ionic motions extending our previous multiscale formalism [34]. In addition to electron dynamics calculations in unit cells of a crystalline solid, we introduce the classical lattice dynamics calculations using the Ehrenfest approximation. We here describe the formalism emphasizing extensions from the previous one. An overview of our formalism is presented in Fig. 1.

A. Macroscopic description

As in ordinary electromagnetism in macroscopic media, we separate two spatial scales. In optical phenomena, a wavelength of a pulsed light that is the order of μm sets the macroscopic spatial scale. Motions of electrons and ions induced by the light are typically the order of 10^{-1}nm for which we call the microscopic spatial scale.

We start with considering microscopic scalar and vector potentials of the electromagnetic fields. As in our previous development [34], we use the so-called Weyl gauge in which the scalar potential ϕ is set to zero. The Maxwell equations for the vector potential are given as follows:

$$\frac{1}{c^2}\frac{\partial^2}{\partial t^2}\vec{A}(\vec{r},t) - \nabla^2\vec{A}(\vec{r},t) + \vec{\nabla}(\vec{\nabla}\cdot\vec{A}(\vec{r},t)) = -\frac{4\pi e}{c}(\vec{j}_{\rm e}(\vec{r},t) - \vec{j}_{\rm ion}(\vec{r},t)). \quad (1)$$

We denote number current densities of electrons and ions as $\vec{j}_{\rm e}$ and $\vec{j}_{\rm ion}$, respectively. We will describe electronic motion by the TDDFT and ionic motion by Newtonian mechanics.

We separate the vector potential into macroscopic and microscopic components utilizing the usual course-graining procedure. In the following, we introduce a macroscopic coordinate $\mathbf{R}$ to express spatial dependence of macroscopic quantities. For example, the macroscopic vector potential is expressed as $\vec{A}_{\mathbf{R}}(t)$. The equation for $\vec{A}_{\mathbf{R}}(t)$ is given as

$$\frac{1}{c^2}\frac{\partial^2}{\partial t^2}\vec{A}_{\mathbf{R}}(t) - \nabla^2_{\mathbf{R}}\vec{A}_{\mathbf{R}}(t) + \vec{\nabla}_{\mathbf{R}}(\vec{\nabla}_{\mathbf{R}}\cdot\vec{A}_{\mathbf{R}}(t)) = -\frac{4\pi e}{c}(\vec{J}_{{\rm e},\mathbf{R}}(t) - \vec{J}_{{\rm ion},\mathbf{R}}(t)), \quad (2)$$

where $\vec{J}_{{\rm e},\mathbf{R}}$ and $\vec{J}_{{\rm ion},\mathbf{R}}$ express macroscopic counterparts of $\vec{j}_{\rm e}$ and $\vec{j}_{\rm ion}$, respectively. The relations between $\vec{J}_{{\rm e},\mathbf{R}}$ and $\vec{j}_{\rm e}$, and $\vec{J}_{{\rm ion},\mathbf{R}}$ and $\vec{j}_{\rm ion}$ will be shown later.

B. Microscopic description

To solve the macroscopic Eq. (2), we need to establish a relation between the vector potential $\vec{A}_{\mathbf{R}}(t)$ and the current densities, $\vec{J}_{{\rm ion},\mathbf{R}}(t)$ and $\vec{J}_{{\rm e},\mathbf{R}}(t)$. For this purpose, we introduce several approximations and assumptions in the microscopic dynamics.

We first introduce a locally uniform approximation as described below that should be justified by the different spatial scales between the macroscopic and the microscopic dynamics. At each point $\mathbf{R}$, we consider a uniform and infinitely periodic system and calculate microscopic dynamics of electrons and ions under a spatially uniform electric field, $\vec{E}(t) = -(1/c)d\vec{A}_{\mathbf{R}}(t)/dt$, where $\mathbf{R}$ is regarded as a parameter in the microscopic dynamics. Second, we assume that the transverse component of the vector potential can be ignored in the microscopic dynamics. We then express the microscopic electric field around $\mathbf{R}$ using a scalar potential $\phi_{\mathbf{R}}(\vec{r},t)$ instead of the vector potential, which has the same periodicity as the lattice in the microscopic scale. Third, we assume that the medium can be treated as charge-neutral in the microscopic calculations.

Recently, we have examined the validity of the assumptions mentioned above by comparing calculations with and without the assumptions for thin films of silicon [36]. There we compared calculations solving the Maxwell and the TDKS equations simultaneously using spatial grids of different (multiple) scales and common (single) scale. The results indicate that both calculations coincide with each other in high accuracy for films of thickness equal to or larger than 5 nm.

Under the above assumptions and approximations, the microscopic dynamics of electrons and ions in a unit cell of the medium is described as follows. The electron dynamics is described by the TDKS equation:

$$i\hbar\frac{\partial}{\partial t}\psi_{i,\mathbf{R}}(\vec{r},t) = \left[\frac{1}{2m}\left\{-i\hbar\vec{\nabla}_{\vec{r}} + \frac{e}{c}\vec{A}_{\mathbf{R}}(t)\right\}^2 - e\phi_{\mathbf{R}}(\vec{r},t) + \frac{\delta E_{XC}[n_{e,\mathbf{R}}]}{\delta n_{e,\mathbf{R}}}\right]\psi_{i,\mathbf{R}}(\vec{r},t). \quad (3)$$

As noted above, the vector potential $\vec{A}_{\mathbf{R}}(t)$ is treated as a spatially uniform field in the unit cell. Namely, $\mathbf{R}$ is treated as a parameter, independent of the microscopic coordinate $\vec{r}$. The scalar potential $\phi_{\mathbf{R}}(\vec{r},t)$ follows the Poisson equation,

$$\vec{\nabla}^2_{\vec{r}}\phi_{\mathbf{R}}(\vec{r},t) = -4\pi e[-n_{{\rm e},\mathbf{R}}(\vec{r},t) + n_{{\rm ion},\mathbf{R}}(\vec{r},t)], \quad (4)$$

where $n_{{\rm e},\mathbf{R}}(\vec{r},t)$ and $n_{{\rm ion},\mathbf{R}}(\vec{r},t)$ represent number densities of electrons and ions, respectively. Their expressions will be given later. The scalar potential may be decomposed into Hartree and ionic potentials:

$$-e\phi_{\mathbf{R}}(\vec{r},t) = V_{H,\mathbf{R}}(\vec{r},t) + V_{{\rm ion},\mathbf{R}}(\vec{r},t). \quad (5)$$

For the ionic dynamics, we adopt the Ehrenfest dynamics. Namely, we consider Newtonian dynamics for ions using the

average force produced by the electron density distribution of $n_{\mathrm{e},\mathbf{R}}(\vec{r},t)$. Thus the ionic motion is treated classically in the present framework, and no quantum nature of phonons is taken into account. Denoting the coordinate of the αth ion by $\vec{s}_\alpha$, the Newtonian equation is given by

$$M_\alpha \frac{d^2\vec{s}_{\alpha,\mathbf{R}}}{dt^2} = -\frac{eZ_\alpha}{c}\frac{d\vec{A}_\mathbf{R}}{dt} - \frac{\partial}{\partial \vec{s}_{\alpha,\mathbf{R}}}\int_\Omega d\vec{r}[en_{\mathrm{ion},\mathbf{R}}\phi_\mathbf{R}]. \quad (6)$$

The second term on the right-hand-side can be written in the following form:

$$-\frac{\partial}{\partial \vec{s}_{\alpha,\mathbf{R}}}\int_\Omega d\vec{r}\left[en_{\mathrm{ion},\mathbf{R}}\phi_\mathbf{R}\right] = -\frac{\partial}{\partial \vec{s}_{\alpha,\mathbf{R}}}\left[\sum_\beta \frac{Z_\alpha Z_\beta e^2}{|\vec{s}_{\alpha,\mathbf{R}}-\vec{s}_{\beta,\mathbf{R}}|} - \int_\Omega d\vec{r}\frac{Z_\alpha n_{\mathrm{e},\mathbf{R}}(\vec{r},t)e^2}{|\vec{s}_{\alpha,\mathbf{R}}-\vec{r}|}\right], \quad (7)$$

where β sum runs over all ions. Z_α is the charge number of the αth ion. This expression shows that the force acting on αth ion is given by the sum of the Coulomb force from electrons and other ions, and the force by the macroscopic electric field. In practical calculations, we observe that the second term in Eq. (6) dominates in the stimulated Raman scattering process that will be shown later.

The density and the current density in the microscopic scale are given as follows. For ions, they are given by

$$n_{\mathrm{ion},\mathbf{R}}(\vec{r},t) = \sum_\alpha Z_\alpha \delta\big(\vec{r}-\vec{s}_{\alpha,\mathbf{R}}(t)\big), \quad (8)$$

$$\vec{j}_{\mathrm{ion},\mathbf{R}}(\vec{r},t) = \sum_\alpha Z_\alpha \delta\big(\vec{r}-\vec{s}_{\alpha,\mathbf{R}}(t)\big)\frac{d\vec{s}_{\alpha,\mathbf{R}}}{dt}. \quad (9)$$

For electrons, they are given by

$$n_{\mathrm{e},\mathbf{R}}(\vec{r},t) = \sum_i |\psi_{i,\mathbf{R}}(\vec{r},t)|^2, \quad (10)$$

$$\vec{j}_{\mathrm{e},\mathbf{R}}(\vec{r},t) = \frac{1}{2m}\sum_i \left\{\psi^*_{i,\mathbf{R}}(\vec{r},t)\left[-i\hbar\vec{\nabla}_{\vec{r}} + \frac{e}{c}\vec{A}_\mathbf{R}(t)\right] \times \psi_{i,\mathbf{R}}(\vec{r},t) + c.c\right\}. \quad (11)$$

The macroscopic density and current density are obtained by taking an average over the unit cell volume, Ω. The current density is explicitly given by

$$\vec{J}_{\mathrm{ion},\mathbf{R}}(t) = \frac{1}{\Omega}\int_\Omega d\vec{r}\,\vec{j}_{\mathrm{ion},\mathbf{R}}(\vec{r},t) = \frac{1}{\Omega}\sum_{\alpha\in\Omega} Z_\alpha \frac{d\vec{s}_\alpha}{dt}, \quad (12)$$

$$\vec{J}_{\mathrm{e},\mathbf{R}}(t) = \frac{1}{\Omega}\int_\Omega d\vec{r}\,j_{\mathrm{e},\mathbf{R}}(\vec{r},t). \quad (13)$$

To carry out time evolution calculations for light electromagnetic fields, electrons, and ions, we solve the coupled Eqs. (2), (3), and (6), simultaneously. For the Kohn-Sham orbital $\psi_{i,\mathbf{R}}(\vec{r},t)$, we introduce the time-dependent Bloch orbital $u_{n\vec{k},\mathbf{R}}(\vec{r},t)$ by $\psi_{i,\mathbf{R}}(\vec{r},t) = e^{i\vec{k}\cdot\vec{r}}u_{n\vec{k},\mathbf{R}}(\vec{r},t)$ and solve the equation for $u_{n\vec{k},\mathbf{R}}(\vec{r},t)$ in practice.

In the present scheme, nonlinear effects originated from various physical mechanisms are incorporated. If the electromagnetic fields are strong, the electric field may induce nonlinear electron dynamics in the microscopic scale. Since we solve the TDKS equation without any perturbative approximations, this scheme can treat even extremely nonlinear regimes close to the damage threshold. If the amplitude of the lattice motion is large, nonlinearity arising from anharmonicity of interatomic potential may become significant. The effect is included since we solve the Newtonian equation without harmonic approximation for the ionic motion. If the electromagnetic fields are not very strong and the amplitude of the lattice motion is not substantial, the present scheme is capable of describing ordinary nonlinear optical phenomena involving lattice dynamics such as the stimulated Raman scattering that will be discussed later. Finally, if we freeze the ionic positions and the electromagnetic fields are sufficiently weak, the present scheme results in ordinary electromagnetism with a linear constitutive relation in which the dielectric function is provided from the TDDFT.

C. Lagrangian and conserved energy

It is possible to write a Lagrangian that provides the equations of motion presented in the previous subsection:

$$\begin{aligned} L = \int d\mathbf{R}\Bigg[&\int_\Omega d\vec{r}\sum_i\left\{\psi^*_{i,\mathbf{R}}i\hbar\frac{\partial}{\partial t}\psi_{i,\mathbf{R}} - \frac{1}{2m}\left|\left(-i\hbar\vec{\nabla}_{\vec{r}} + \frac{e}{c}\vec{A}_\mathbf{R}\right)\psi_{i,\mathbf{R}}\right|^2\right\} \\ &- \int_\Omega d\vec{r}\{e(n_{\mathrm{ion},\mathbf{R}}-n_{\mathrm{e},\mathbf{R}})\phi_\mathbf{R} + E_{XC}[n_{\mathrm{e},\mathbf{R}}]\} \\ &+ \frac{1}{8\pi}\int_\Omega d\vec{r}(\vec{\nabla}_{\vec{r}}\phi_\mathbf{R})^2 + \frac{\Omega}{8\pi c^2}\left(\frac{\partial\vec{A}_\mathbf{R}}{dt}\right)^2 \\ &- \frac{\Omega}{8\pi}(\vec{\nabla}_\mathbf{R}\times\vec{A}_\mathbf{R})^2 + \sum_\alpha\frac{M_\alpha}{2}\left(\frac{d\vec{s}_{\alpha,\mathbf{R}}}{dt}\right)^2 \\ &+ \sum_\alpha\frac{Z_\alpha e}{c}\frac{d\vec{s}_{\alpha,\mathbf{R}}}{dt}\cdot\vec{A}_\mathbf{R},\Bigg], \end{aligned} \quad (14)$$

where α sum runs for ions in the unit cell. The variation with respect to the Kohn-Sham orbital $\psi_{i,\mathbf{R}}$ gives the TDKS Eq. (3), the variation with respect to the scalar potential $\phi_\mathbf{R}$ gives the Poisson Eq. (4), the variation with respect to the vector potential $\vec{A}_\mathbf{R}$ gives the wave Eq. (2), and the variation with respect to the ionic coordinate $\vec{s}_{\alpha,\mathbf{R}}$ gives the Newtonian Eq. (6).

One of the advantages of the Lagrangian formalism is that it is possible to construct an expression of the conserved energy:

$$\begin{aligned} E = \int d\mathbf{R}\Bigg[&\int_\Omega d\vec{r}\sum_i\left\{\frac{1}{2m}\left|\left(-i\hbar\vec{\nabla}_{\vec{r}} + \frac{e}{c}\vec{A}_\mathbf{R}\right)\psi_{i,\mathbf{R}}\right|^2\right\} \\ &+ \int_\Omega d\vec{r}\{e(n_{\mathrm{ion},\mathbf{R}}-n_{\mathrm{e},\mathbf{R}})\phi_\mathbf{R} + E_{XC}[n_{\mathrm{e},\mathbf{R}}]\} \end{aligned}$$

$$+\frac{\Omega}{8\pi c^2}\left(\frac{\partial \vec{A}_{\mathbf{R}}}{dt}\right)^2+\frac{\Omega}{8\pi}(\vec{\nabla}_{\mathbf{R}}\times\vec{A}_{\mathbf{R}})^2$$
$$+\sum_\alpha\frac{M_\alpha}{2}\left(\frac{d\vec{s}_{\alpha,\mathbf{R}}}{dt}\right)^2+\sum_\alpha\frac{Z_\alpha e}{c}\frac{d\vec{s}_{\alpha,\mathbf{R}}}{dt}\cdot\vec{A}_{\mathbf{R}}\Bigg] \quad (15)$$

In practical calculations, the conservation of this energy provides a useful check of the accuracy of the calculation.

D. One-dimensional propagation

Later in the present paper, we will show a calculation in which a pulsed light irradiates normally on a thin film. In this setting, the light propagation can be treated as a one-dimensional problem. We denote the one-dimensional macroscopic coordinate as X. We write below the equations for this case.

The Maxwell equation for the macroscopic vector potential $\vec{A}_X(t)$ is expressed as

$$\left[\frac{1}{c^2}\frac{\partial^2}{\partial t^2}-\frac{\partial^2}{\partial X^2}\right]\vec{A}_X(t)=-\frac{4\pi e}{c}[\vec{J}_{\mathrm{e},X}(t)-\vec{J}_{\mathrm{ion},X}(t)]. \quad (16)$$

The current density coming from electron motion is expressed using Kohn-Sham orbitals:

$$\vec{J}_{\mathrm{e},X}(t)=\frac{1}{m\Omega}\int_\Omega d\vec{r}\left\{\psi^*_{i,X}\left[-i\hbar\vec{\nabla}_{\vec{r}}+\frac{e}{c}\vec{A}_X(t)\right]\psi_{i,X}\right\}. \quad (17)$$

The current density coming from ionic motion is given by

$$\vec{J}_{\mathrm{ion},X}(t)=\frac{1}{\Omega}\sum_{\alpha\in\Omega}Z_\alpha\frac{d\vec{s}_{\alpha,X}}{dt}. \quad (18)$$

The TDKS equation for $\psi_{i,X}$ is given as

$$i\hbar\frac{\partial}{\partial t}\psi_{i,X}(\vec{r},t)=\left[\frac{1}{2m}\left\{-i\hbar\vec{\nabla}_{\vec{r}}+\frac{e}{c}\vec{A}_X(t)\right\}^2-e\phi_X(\vec{r},t)+\frac{\delta E_{XC}[n_{e,X}]}{\delta n_{e,X}}\right]\psi_{i,X}(\vec{r},t), \quad (19)$$

The Poission equation is given by

$$\nabla^2\phi_X=4\pi e[n_{\mathrm{e},X}-n_{\mathrm{ion},X}]. \quad (20)$$

Finally, the Newtonian equation for $\vec{s}_{\alpha,X}$ is

$$M_\alpha\frac{d^2\vec{s}_{\alpha,X}}{dt^2}=-\frac{eZ_\alpha}{c}\frac{d\vec{A}_X}{dt}-\frac{\partial}{\partial\vec{s}_{\alpha,X}}\int_\Omega d\vec{r}[en_{\mathrm{ion},X}\phi_X]. \quad (21)$$

III. SETUP OF SIMULATION SYSTEM AND NUMERICAL DETAILS

A. Coherent phonon and impulsively stimulated Raman scattering spectroscopy

To demonstrate how the method works in typical nonlinear optical phenomena in crystalline solids, we apply the method to describe a pump-probe measurement of coherent optical phonons [19]. Coherent phonons are generated by an irradiation of a strong and ultrashort laser pulse on condensed media. They are characterized by coherent lattice motion in a macroscopic spatial area with a common phase. We consider the case in which the pulse frequency is below the band-gap energy. In that case, the driving force of the phonon is an impulsive force that is generated by a virtual and temporal change of the electronic state and that only exerts during the irradiation of the pulse. To excite the lattice dynamics by the impulsive force, the pulse duration must be much shorter than the period of the optical phonon. This nonlinear process of the coherent phonon generation is known as the ISRS mechanism.

As a material, we consider a diamond thin film. Two ultrashort pulses with the same frequency $\omega = 1.55$ eV$/\hbar$, which is well below the band gap of the diamond, are successively irradiated normally on the surface along the [100] axis. The pulse has a cosine-square envelope with the full time duration of 18 fs, which corresponds to 6.5 fs in full width at half maximum (FWHM). This is shorter than the period of the optical phonon of diamond, which is about 25 fs.

First, a strong pump pulse that is linearly polarized along the [011] direction is irradiated. It generates the coherent optical phonon with atomic displacements in the [100] direction. Next, a weak probe pulse that is polarized along the [010] direction is used to detect the coherent phonon. Accompanying the probe pulse, an impulsively stimulated Raman-scattered wave that is polarized along the [001] direction is generated and amplified by the nonlinear interaction between the lattice motion and the probe pulse. Usually, this process is described using the Raman tensor of the diamond [37]. Our simulation automatically includes the effect solving the dynamical equations. The Raman wave as well as the propagated probe pulse appear as transmission signals after they get out of the thin film.

The light propagation in the present setting can be described by the one-dimensional equations presented in Sec. II D. In the calculation, we set the crystalline *abc* axes of the cubic diamond to coincide with the *xyz* axes of the Cartesian coordinates, respectively.

Although it is in principle possible to carry out calculations of the pump and the probe pulse propagations in a single calculation, we separate them in two to avoid the complexity coming from the reflection of the pump pulse at the back surface of the thin film. First, we carry out the calculation of the pump pulse, aiming to describe the generation of the coherent optical phonon. At this stage, we carry out the calculation for a sufficiently thick film so no reflections appear at the back surface. In practice, we make a calculation for a diamond thin film of 10 μm thickness and for a time duration of 80 fs. At the end of this calculation, the pump pulse locates in the spatial region $6\ \mu\mathrm{m} < X < 10\ \mu\mathrm{m}$. We extract the lattice dynamics of the spatial region $0 < X < 6\ \mu$m from this calculation and use it in the next calculation of the probe stage.

For the probe-stage calculation, we consider a thin film of 6 μm thickness. The probe simulation starts with the following initial condition: First, we set the positions of ions at each macroscopic grid point to the final positions of the pump-stage calculation. We also set the initial velocity of ions. Then, electronic ground-state calculation is carried out for the shifted ionic positions at each macroscopic point. The probe pulse is then irradiated at the surface.

For the vector potential of the incident pulses, we use the following time profile. For the pump pulse, it is given by

$$\vec{A}_{\rm pump}(t) = \vec{e}_{[011]} A_0^{\rm pump} \cos^2\left(\frac{\pi t}{T}\right) \cos \omega t, \quad (0 < t < T), \tag{22}$$

where $\vec{e}_{[011]}$ is the unit vector of the polarization direction, $A_0^{\rm pump}$ specifies the amplitude, T specifies the full duration, and ω specifies the average frequency. The probe pulse is given by a similar expression. As mentioned previously, the polarization direction of $\vec{e}_{[010]}$ is used, and we choose the common frequency $\omega = 1.55$ eV/$\hbar$ and the pulse duration $T = 18$ fs for the pump and the probe pulses. Some other pump frequencies are also used later. The amplitude $A_0^{\rm pump}$ and $A_0^{\rm probe}$ are so chosen that the maximum intensity of the incident pump pulse is 2×10^{12} W/cm^2 and that of the probe pulse is 1×10^{10} W/cm^2. The probe pulse is sufficiently weak so that there occurs no significant nonlinear effects related to the intensity of the probe pulse and that it brings any changes in the lattice dynamics.

The vector potential is initially set to

$$\vec{A}_X(t) = \vec{A}_{\rm pump}\left(t - \frac{X}{c}\right) \tag{23}$$

for the pump-stage calculation, and set to

$$\vec{A}_X(t) = \vec{A}_{\rm probe}\left(t - \frac{X}{c} - \tau\right) \tag{24}$$

for the probe-stage calculation, where τ specifies the time difference between the pump and the probe pulses.

For the exchange-correlation potential, we adopt the adiabatic local density approximation (ALDA). It is well known that ALDA has deficiencies in describing optical responses of dielectrics, such as the underestimation of the band-gap energies. However, since the present paper aims to demonstrate the feasibility of the calculation including lattice motion, we adopt the ALDA as the simplest choice. We also note that there exist exchange-correlation effects that can only be treated using a vector potential, as formulated in the time-dependent current density-functional theory [38,39]. We ignore the contribution for simplicity in the present paper.

To describe microscopic electron motion in a unit cell, norm-conserving pseudpotential [40] is used for the electron-ion interaction with a separable approximation [41]. It should be noted that the nonlocal component of the pseudopotential inducesan additional contribution in the electron current density in Eq. (11) [42].

To show the quality of the microscopic calculation, we show the dielectric function of the diamond calculated by linear response TDDFT. In the calculation, the same real-time numerical scheme as that used for the microscopic electron dynamics calculation is used to obtain the dielectric function. The result is shown in Fig. 2. Although the band gap is substantially underestimated in the ALDA, an overall shape of the dielectric function is in reasonable agreement with the experimental data. At frequency region below 1 eV, a tiny structure is seen in the imaginary part. This is not physical since the band gap of the diamond is 4.8 eV in the LDA and comes from a numerical artifact of the calculation of a finite time period.

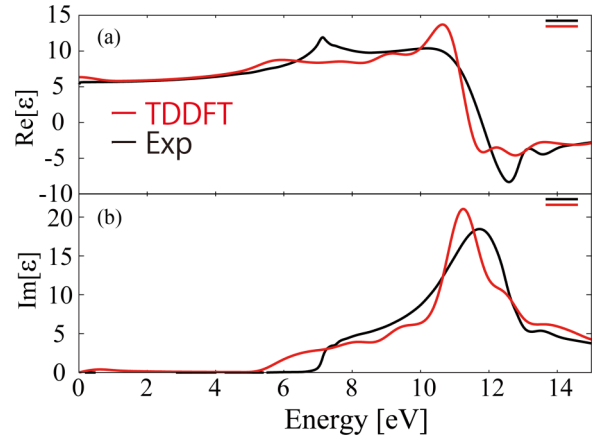

FIG. 2. Calculated (a) real and (b) imaginary parts of the dielectric function of diamond (the red lines). The experimental measurements [43] (the black lines) are also plotted as a reference.

B. Numerical details

We implement our method to the open source software SALMON [44] that is developed mainly in our research group. SALMON is downloadable from our website [45].

In the one-dimensional macroscopic space, the X coordinate is discretized using the spacing of 15 nm. For a film of 6 μm thickness, 400 macroscopic grid points are employed. At each macroscopic grid point, we prepare a microscopic grid system. The cubic unit cell of the diamond used in the present paper includes eight carbon atoms. The side length of the cubic unit cell that is equal to 3.567 Å is discretized into 16 spatial grid points. The Brillouin zone is discretized into uniform grids of 12^3 k points. The three equations of motion are integrated with the common time step of 2 as. We note that the microscopic Kohn-Sham Hamiltonian needs to be updated. While the Hartree potential is updated every time step, the ionic potential is updated every five time steps. This is because the ionic displacement is very small as we see below and the update of the nonlocal pseudopotential requires large computational resources.

Our approach is computationally expensive since calculations of the microscopic electronic and ionic dynamics are required on a number of macroscopic grid points. Therefore, efficient parallelization is essential to carry out the calculation. We employ a hybrid parallelization scheme using both MPI and OpenMP parallelizations. We use a supercomputer Oakforest-PACS operated jointly by University of Tokyo and University of Tsukuba. It is composed of next-generation Intel Xeon-Phi many-core processors (68 cores/node). In our typical calculation using 400 macroscopic grid points, we utilize 400 nodes of the Oakforest-PACS. By MPI parallelization, each node carries out calculations of microscopic dynamics of one macroscopic grid point. Inside the node, MPI parallelization is again adopted for k points. OpenMP is then adopted for the calculations of electron orbitals. A typical time evolution calculation of 80 fs costs about 10 h using 400 nodes.

IV. PUMP-PROBE SIMULATIONS

A. Pump process: Coherent phonon generation

We first show the calculation for the generation of coherent phonons in diamond by the pump pulse. Figure 3(a) shows the propagation of the pump light by red lines and the displacement of the ions at different macroscopic points of X by green-filled circles. When the field enters the medium, first the ions at the left edge point of the medium start to move by the light-matter interaction. After that, as the pump pulse propagates through the medium, the harmonic motion of ions is generated in turn at each macroscopic grid point. In Fig. 3(a), a wavelike behavior of the ionic displacement is seen along the X axis. The amplitude of the ionic displacement is rather small, typically 10^{-4} Å. This reflects the fact that there is no resonant energy transfer from the pump pulse to electrons since the pulse frequency is much below the band-gap energy.

It is noted that the wavelike bahavior is not an ordinary propagation of the lattice wave. The period of the oscillation at each X point is equal to the period of the optical phonon, 25 fs for diamond. However, since the wave is generated by the pump pulse that propagates with the speed of light in the medium, c/n, with the index of refraction n, the front edge of the wave moves with the same speed. This is orders of magnitude larger than the phase velocity of the lattice wave which is determined by the phonon dispersion curve. The amplitude of the oscillation does not attenuate in the medium since the pump pulse is not absorbed during the propagation. Although there is a small energy transfer from the pulsed light to the lattice motion, the energy transfer is very small as will be shown later.

In Fig. 3(b), the generation processes of the optical phonon at $X = 0$ and 2 μm are shown as a function of time. We first look at the case of $X = 0$ μm. Immediately after the light electric field arrives at the position, the force that is proportional to the square of the electric field appears. It then generates the ionic displacement corresponding to the coherent phonon. As the ions start to move, the restoring force begins to work. The ionic displacements show a sine shape at times after the center of the pump-pulse envelope (i.e., $t >$ 9 fs). These behaviors of the force and the generation process of the coherent phonon is consistent with the picture of the ISRS mechanism [19]. After the pump field passes away, a simple harmonic motion of ions continues without decay. The same generation process is seen at $X = 2$ μm in Fig. 3(b) after the pump field arrives at the position.

The driving force for ions is generated through the change in the electron density, not from the direct field-ion interaction. In Figs. 3(c) and 3(d), electron density in the (011) plane of diamond is shown for the ground state in Fig. 3(c) and changes in density at times $t = 4.0$ fs, 8.0 fs, and 8.6 fs in Fig. 3(d). In the ground state, the covalent bonds appear between ions as seen in Fig. 3(c). The pump field induces a shift of bonding electrons along the bond direction toward the direction of the electric field. The larger changes in the density are observed under the stronger field. Although the direction of the shift of electrons changes when the direction of the field becomes opposite, the direction of the force on ions does not change because all bonds in the (011) plane are weakened irrespective of the direction of the electric field. This gives rise to the driving force of ions along the [100] axis during the pump pulse.

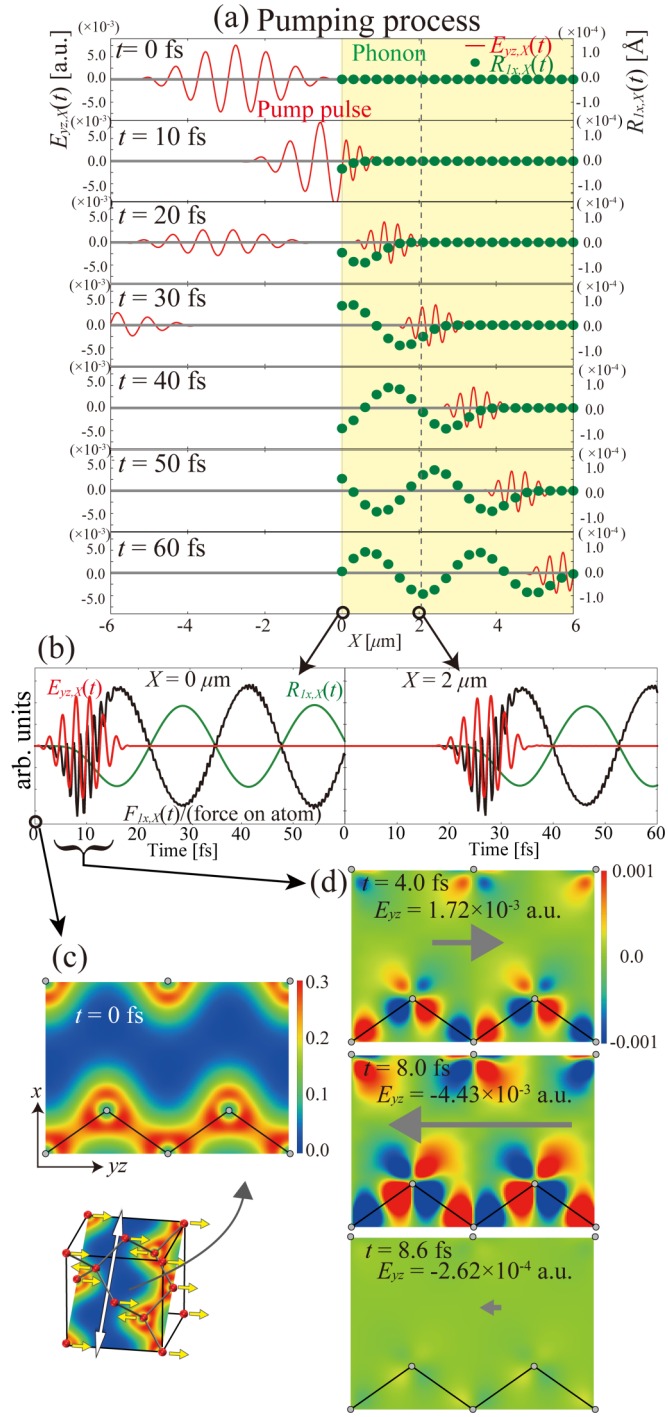

FIG. 3. (a) Snapshots of the electric field of the pump pulse (red lines) and the ionic displacement (green filled circles) are shown along the macroscopic grid points of X coordinate. (b) Electric field of the pump pulse (red line), the force acting on the ion (black line), and the ionic displacement (green line) are shown as a function of time at $X = 0$ and 2 μm. (c) The ground-state electron density in the (011) plane of the unit cell. (d) The changes in the electron density from the ground state are shown at $t = 4.0$, 8.0, and 8.6 fs at $X = 0$ μm.

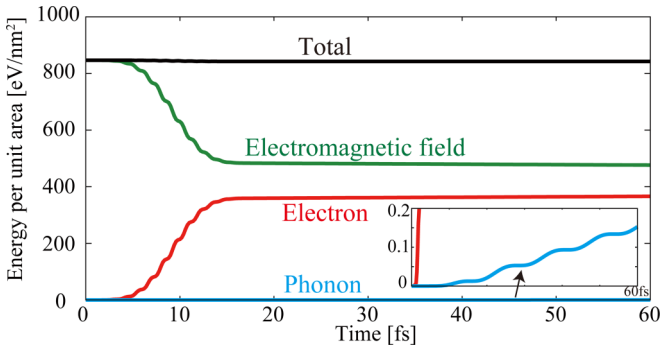

FIG. 4. Energies per unit area integrated over the propagation direction are shown as a function of time during the propagation of the pump pulse. The total energy (the black line) is decomposed into the energy of the electromagnetic field (the green line), the energy of electronic excitations (the red line), and the kinetic energy of the ions (the blue line).

In Fig. 4, the energy per unit area is shown as a function of time during the pump-pulse propagation. The energy components of the electromagnetic fields, electronic excitations, and lattice motions as well as the total energy that is the sum of the three energies are shown. When the light pulse gets into the medium, the energy components start to change in time. After the light pulse fully gets into the medium region, the energy components change very little. The lattice energy is always small because the amplitude of the lattice motion is small, as was seen in Fig. 3. Magnifying the plot of the energy of the lattice motion, a stepwise increase of energy is observed. This reflects the fact that the lattice motion takes place in more wide spatial regions as the pump pulse propagates through the medium. During the process, the conservation of the total energy is satisfied in high accuracy, supporting the numerical accuracy of the calculation.

B. Different pump-pulse frequencies

We next show in Fig. 5 the generation of coherent phonons by pump pulses of three different frequencies. In the calculations, smaller macroscopic grid spacing is used for shorter wavelengths of the pump pulse in the medium, 15, 10, and 5 nm in (a), (b), and (c), respectively. Figure 5(a) shows the generation with $\omega = 1.55$ eV$/\hbar$, the same as that shown in Fig. 3(a). Figure 5(b) shows the generation with $\omega = 3.5$ eV$/\hbar$. Although the pump frequency is still below the optical gap energy, the phonon amplitude decays with X, whereas the amplitude of the lattice oscillation at each X point does not decay with time. This is caused by the attenuation of the pump pulse as it propagates through the medium. Since the pump pulse is rather strong with the intensity, 2×10^{12} W/cm^2, the pump pulse excites electrons by the two-photon absorption process and loses the energy as it propagates through the medium. Although the same intensity is used for the case of $\omega = 1.55$ eV$/\hbar$, no absorption is seen because at least four photons are required to exceed the band-gap energy.

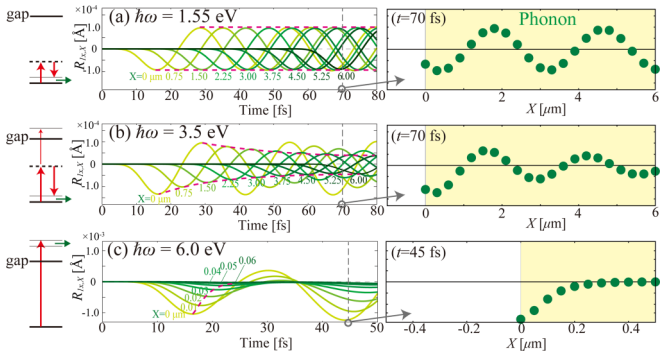

FIG. 5. Coherent phonon generation by pump pulses of three different frequencies, $\hbar\omega =$ (a) 1.55, (b) 3.5, and (c) 6.0 eV. Ionic displacements as a function of time are shown at selected macroscopic points of X (the left panels) and those along the coordinate X at specific times (the right panels). Note that the vertical and horizontal scale of (c) is different from those of (a) and (b).

At $\omega = 6$ eV$/\hbar$ that is above the optical gap energy, the amplitude of the lattice motion at the surface is one order of magnitude larger than the nonresonant cases, as seen in Fig. 5(c), The displacement of ions shows a harmonic motion of the cosine shape, namely the oscillation takes place around the shifted equilibrium position. This is due to the change of the generation mechanism of coherent phonons, from ISRS to the displacive excitations of coherent phonon (DECP) [19]. Thus, the coherent phonons by both ISRS and DECP mechanisms can be described in the present formalism. These results are consistent with Ref. [33], where generation mechanisms of coherent phonons are discussed using TDDFT without coupling to the light propagation. The amplitude of the lattice motion decays with X since the field attenuates by the absorption of the pulse.

C. Probe process: Generation and amplification of stimulated Raman wave

We next proceed to the simulations for the propagation of probe pulses. As mentioned previously, we make separate calculations from those of the pump pulse that generates the coherent phonon.

The polarization of the probe pulse is set to [010] direction. The time delay between the pump and the probe pulses are specified by τ in Eq. (24). Two simulations are performed with $\tau = 83.0$ and 89.5 fs. We note that the calculation of the pump stage ends at $t = 80$ fs. In the calculation of $\tau = 83.0$ fs, the ionic displacement at the surface is maximum when the probe pulse reaches the surface of the medium. In the calculation of $\tau = 89.5$ fs, the ionic displacement at the surface is almost zero when the probe pulse reaches the surface of the medium.

In Fig. 6(a), the propagation of the probe pulse as well as the generation of the impulsive stimulated Raman wave are shown for the case of the pump-probe time delay of $\tau = 83.0$ fs. As seen from the figure, the probe pulse shown by the red line propagates with the same speed as the wave of the ionic displacement, at the position of the maximum ionic displacement. This is because the lattice motion proceeds with the speed of the pump pulse, c/n, as noted previously, and the probe pulse also propagates with the same speed since we chose the same frequency for the pump and the probe pulses.

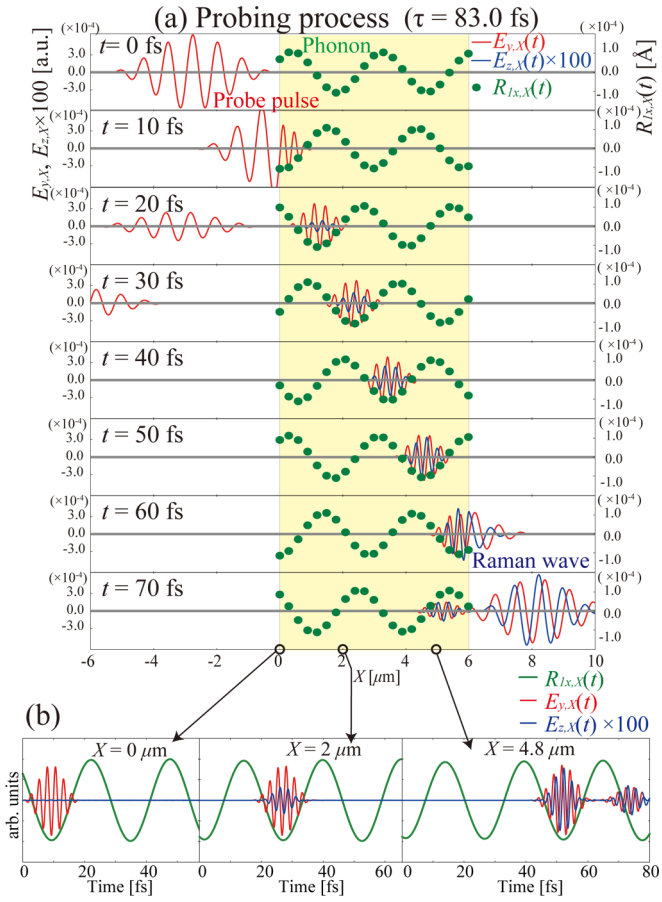

FIG. 6. Simulation results of the probe process with $\tau = 83$ fs. (a) Snapshots of the electric field of the probe pulse in [010] (red line) and in [001] (blue line) directions, and the ionic displacement (green filled circles) are shown along the macroscopic coordinate X. (b) Plots of the same quantities as a function of time at $X = 0$, 2, and 4.8 μm. The time t is set to 0 when the front edge of the probe pulse reaches the surface of the medium.

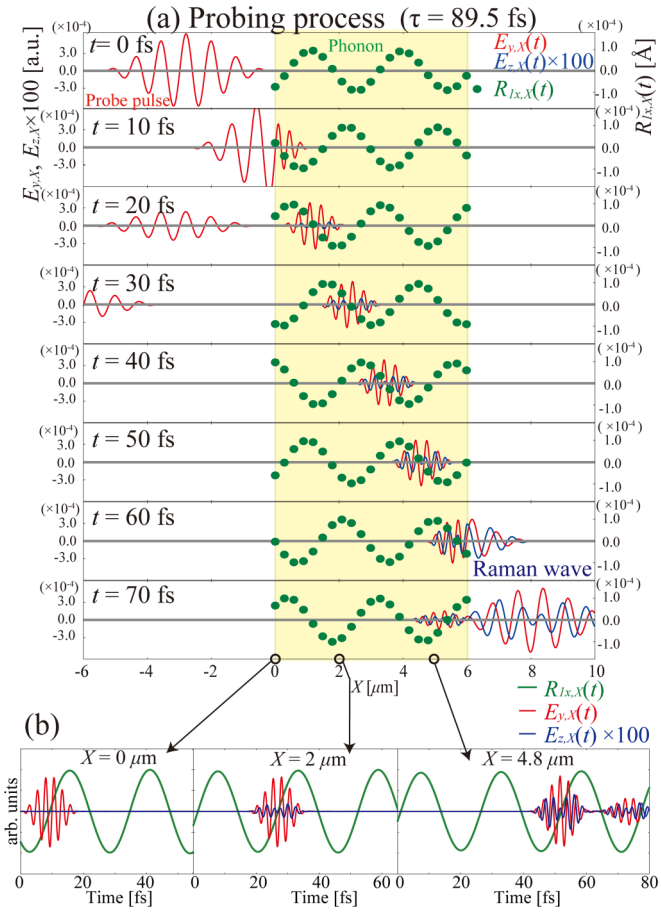

FIG. 7. Simulation results of the probe process with $\tau = 89.5$ fs. Same plots as those in Fig. 6.

During the propagation of the probe pulse, the stimulated Raman wave that is shown by the blue line appears in the [001] direction, perpendicular to both directions of the ionic displacements and the probe polarization. The stimulated Raman wave has the phase shift of $\pi/2$ with respect to the probe pulse, and its amplitude increases linearly with the traveled distance. These features are consistent with the standard theoretical description for the stimulated Raman scattering using the property of the Raman tensor [19,46].

The probe pulse and the stimulated Raman wave as a function of time are shown at $X = 0$, 2, and 4.8 μm in Fig. 6(b). It is seen that two waves exist in the timing of the maximum displacement of the ions and have almost the same envelope shape with common center positions. At $X = 4.8$ μm, the probe and the stimulated Raman waves reflected at the back surface of the medium are seen around $t = 75$ fs.

In Fig. 7(a), the propagation of the probe pulse with the time delay of $\tau = 89.5$ fs is shown. Here, the probe pulse moves with the nodal point of the lattice motion during the propagation in the medium. As is seen from the figure, there appears a clear difference in the pulse shape of the stimulated Raman scattering wave from that of the case of $\tau = 83.0$ fs.

In Fig. 8, we show the pulse shape of the transmitted waves in time domain for the two cases of different time delays.

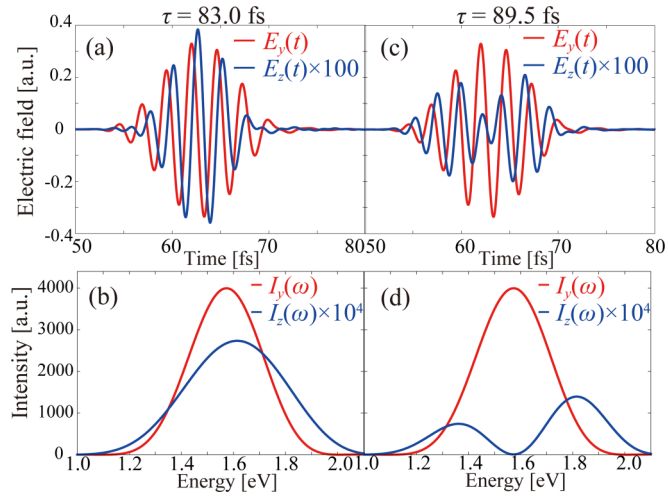

FIG. 8. Transmitted probe $[E_y(t)]$ and stimulated Raman waves $[E_z(t)]$ in the right vacuum region for $\tau = 83.0$ fs are shown in (a), and their power spectra are shown in (b). Those with $\tau = 89.5$ fs are shown in (c) and (d).

Figures 8(a) and 8(c) are the cases of $\tau = 83.0$ and 89.5 fs, respectively. In the case of $\tau = 83.0$ fs, the pulse shape of the stimulated Raman wave $[E_z(t)]$ is similar to the shape of the probe pulse $[E_y(t)]$ except for the phase difference of $\pi/2$. On the other hand, in the case of $\tau = 89.5$ fs, the pulse shape of the stimulated Raman wave is very different from the shape of the probe pulse. This difference can be understood as originating from the difference of the electric current density that produced the stimulated Raman wave. The electric current density that produces the Raman wave is given by $J_{\mathrm{Raman}}(t) \propto Q(t)E_{\mathrm{probe}}(t)$ [19,46], where $E_{\mathrm{probe}}(t)$ is the electric field of the probe pulse and $Q(t)$ is the phonon amplitude that is expressed by the linear combination of the ionic displacements. When the probe pulse enters the medium at the maximum of the phonon amplitude, $Q(t)$ may be regarded as roughly a constant and $J_{\mathrm{Raman}}(t)$ has a similar time profile to that of $E_{\mathrm{probe}}(t)$ since the half period of the lattice motion is assumed to be longer than the duration of the probe pulse. However, when the probe pulse moves with the nodal position of the lattice motion, the phonon amplitude may be approximated by a linear function of time. Then, we have $J_{\mathrm{Raman}}(t) \propto tE_{\mathrm{probe}}(t)$, and the lattice motion produces one extra node to the electric current density. This explains the shape change of the stimulated Raman wave shown in Fig. 8(c).

We show the power spectra of the stimulated Raman waves in Figs. 8(b) and 8(d). Reflecting the different profiles in time domain, they show distinct structures: the double-peak structure appears in the power spectrum of the stimulated Raman wave when it propagates at the nodal point of the lattice motion. We note that such a double-peak structure is indeed related to the recent pump-probe measurement of the coherent phonon in diamond and other insulators [14,17]. We will report our analysis for this problem in a separate publication.

V. SUMMARY

We have developed a computational approach for nonlinear light-matter interaction in solids involving lattice motion based on first-principles TDDFT. A multiscale scheme is developed simultaneously solving the Maxwell equations for light propagation, the TDKS equation for electrons, and the Newtonian equation for ions. As a test example, a pump-probe measurement of coherent phonon generation in diamond is simulated where an amplification of the stimulated Raman wave is observed for the probe stage. It is shown that substantially different shapes of the stimulated Raman waves are obtained, depending on the pump-probe time delays. We expect the method will be useful for a wide phenomena of nonlinear and ultrafast optics in solids.

ACKNOWLEDGMENTS

We acknowledge support by JST-CREST under Grant No. JP-MJCR16N5, and by MEXT as a priority issue theme 7 to be tackled by using Post-K Computer, and by JSPS KAKENHI Grant No. 15H03674. Calculations are carried out at Oakforest-PACS at JCAHPC through the Multidisciplinary Cooperative Research Program in CCS, University of Tsukuba, and through the HPCI System Research Project (Project No. hp180088).

[1] R. W. Boyd, *Nonlinear Optics*, 3rd ed. (Academic Press, Inc., Orlando, FL, 2008).
[2] Y. R. Shen, *The Principles of Nonlinear Optics*, 1st ed. (Wiley-Interscience, Hoboken, New Jersey, 1984).
[3] N. Bloembergen, *Nonlinear Optics*, 4th ed. (World Scientific, Singapore, 1996).
[4] J. W. Goodman, *Introduction to Fourier Optics*, 3rd ed. (Roberts & Company Publishers, Englewood, CO, 2005).
[5] E. Hecht, *Optics*, 4th ed. (Pearson Education, Inc., San Francisco, CA, 2002).
[6] F. Krausz and M. Ivanov, Attosecond physics, Rev. Mod. Phys. **81**, 163 (2009).
[7] F. Calegari, G. Sansone, S. Stagira, C. Vozzi, and M. Nisoli, Advances in attosecond science, J. Phys. B **49**, 062001 (2016).
[8] S. Ghimire, A. D. DiChiara, E. Sistrunk, P. Agostini, L. F. DiMauro, and D. A. Reis, Observation of high-order harmonic generation in a bulk crystal, Nat. Phys. **7**, 138 (2011).
[9] T. T. Luu, M. Garg, S. Yu. Kruchinin, A. Moulet, M. Th. Hassan, and E. Goulielmakis, Extreme ultraviolet high-harmonic spectroscopy of solids, Nature **521**, 498 (2015).
[10] M. Schultze, K. Ramasesha, C. D. Pemmaraju, S. A. Sato, D. Whitmore, A. Gandman, James S. Prell, L. J. Borja, D. Prendergast, K. Yabana, D. M. Neumark, and S. R. Leone, Attosecond band-gap dynamics in silicon, Science **346**, 1348 (2014).
[11] A. Sommer, E. M. Bothschafter, S. A. Sato, C. Jakubeit, T. Latka, O. Razskazovskaya, H. Fattahi, M. Jobst, W. Schweinberger, V. Shirvanyan, V. S. Yakovlev, R. Kienberger, K. Yabana, N. Karpowicz, M. Schultze, and F. Krausz, Attosecond nonlinear polarization and light-matter energy transfer in solids, Nature **534**, 86 (2016).
[12] M. Lucchini, S. A. Sato, A. Ludwig, J. Herrmann, M. Volkov, L. Kasmi, Y. Shinohara, K. Yabana, L. Gallmann, and U. Keller, Attosecond dynamical Franz-Keldysh effect in polycrystalline diamond, Science **353**, 916 (2016).
[13] M. Hase, M. Kitajima, A. M. Constantinescu, and H. Petek, The birth of a quasiparticle in silicon observed in time-frequency space, Nature **426**, 51 (2003).
[14] K. Mizoguchi, R. Morishita, and G. Oohata, Generation of Coherent Phonons in a CdTe single Crystal Using an Ultrafast Two-Phonon Laser-Excitation Process, Phys. Rev. Lett. **110**, 077402 (2013).
[15] I. Katayama, K. Sato, S. Koga, J. Takeda, S. Hishita, H. Fukidome, M. Suemitsu, and M. Kitajima, Coherent nanoscale optical-phonon wave packet in graphene layers, Phys. Rev. B **88**, 245406 (2013).
[16] K. Sato, K. Tahara, Y. Minami, I. Katayama, M. Kitajima, H. Kawai, K. Yanagi, and J. Takeda, Resonance enhancement of first- and second-order coherent phonons in metallic single-walled carbon nanotubes, Phys. Rev. B **90**, 235435 (2014).

[17] K. G. Nakamura, K. Ohya, H. Takahashi, T. Tsuruta, H. Sasaki, S. Uozumi, K. Norimatsu, M. Kitajima, Y. Shikano, and Y. Kayanuma, Spectrally resolved detection in transient-reflectivity measurements of coherent optical phonons in diamond, Phys. Rev. B **94**, 024303 (2016).

[18] H. Sasaki, R. Tanaka, Y. Okano, F. Minami, Y. Kayanuma, Y. Shikano, and K. G. Nakamura1, Coherent control theory and experiment of optical phonons in diamond, Sci. Rep. **8**, 9609 (2018).

[19] R. Merlin, Generating coherent THz phonons with light pulses, Solid State Commun. **102**, 207 (1997).

[20] T. E. Stevens, J. Kuhl, and R. Merlin, Coherent phonon generation and the two stimulated Raman tensors, Phys. Rev. B **65**, 144304 (2002).

[21] C. Thomsen, J. Strait, Z. Vardeny, H. J. Maris, J. Tauc, and J. J. Hauser, Coherent Phonon Generation and Detection by Picosecond Light Pulses, Phys. Rev. Lett. **53**, 989 (1984).

[22] G. C. Cho, W. Kütt, and H. Kurz, Subpicosecond Time-Resolved Coherent-Phonon Oscillations in GaAs, Phys. Rev. Lett. **65**, 764 (1990).

[23] K. Iwano, Y. Shimoi, T. Miyamoto, D. Hata, M. Sotome, N. Kida, S. Horiuchi, and H. Okamoto, Ultrafast Photoinduced Electric-Polarization Switching in a Hydrogen-Bonded Ferroelectric Crystal, Phys. Rev. Lett. **118**, 107404 (2017).

[24] S. Horiuchi, K. Kobayashi, R. Kumai, and S. Ishibashi, Proton tautomerism for strong polarization switching, Nat. Commun. **8**, 14426 (2017).

[25] T. Frigge, B. Hafke, T. Witte, B. Krenzer, C. Streubühr, A. Samad Syed, V. Mikšić Trontl, I. Avigo, P. Zhou, M. Ligges, D. von der Linde, U. Bovensiepen, M. Horn-von Hoegen, S. Wippermann, A. Lücke, S. Sanna, U. Gerstmann, and W. G. Schmidt, Optically excited structural transition in atomic wires on surfaces at the quantum limit, Nature **544**, 207 (2017).

[26] M. F. Jager, C. Ott, P. M. Kraus, C. J. Kaplan, Winston Pouse, Robert E. Marvel, Richard F. Haglund, Daniel M. Neumark, and Stephen R. Leone, Tracking the insulator-to-metal phase transition in VO_2 with few-femtosecond extreme UV transient absorption spectroscopy, PNAS **114**, 9558 (2017).

[27] R. M. Martin, *Electronic Structure: Basic Theory and Practical Methods* (Cambridge University Press, Cambridge, 2004).

[28] C. A. Ullrich, *Time-Dependent Density-Functional Theory: Concepts and Applications*, Oxford Graduate Texts (Oxford University Press, Oxford, 2012).

[29] M. A. L. Marques, N. T. Maitra, F. M. S. Nogueira, E. K. U. Gross, and A. Rubio, editors, *Fundamentals of Time-Dependent Density Functional Theory, 2012 edition*, Lecture Notes in Physics (Springer, Berlin, Heidelberg, 2012).

[30] E. Runge and E. K. U. Gross, Density-Functional Theory for Time-Dependent Systems, Phys. Rev. Lett. **52**, 997 (1984).

[31] K. Yabana and G. F. Bertsch, Time-dependent local-density approximation in real time, Phys. Rev. B **54**, 4484 (1996).

[32] T. Otobe, M. Yamagiwa, J.-I. Iwata, K. Yabana, T. Nakatsukasa, and G. F. Bertsch, First-principles electron dynamics simulation for optical breakdown of dielectrics under an intense laser field, Phys. Rev. B **77**, 165104 (2008).

[33] Y. Shinohara, K. Yabana, Y. Kawashita, J.-I. Iwata, T. Otobe, and G. F. Bertsch, Coherent phonon generation in time-dependent density functional theory, Phys. Rev. B **82**, 155110 (2010).

[34] K. Yabana, T. Sugiyama, Y. Shinohara, T. Otobe, and G. F. Bertsch, Time-dependent density functional theory for strong electromagnetic fields in crystalline solids, Phys. Rev. B **85**, 045134 (2012).

[35] B. F. E. Curchod, U. Rothlisberger, and I. Tavernelli, Trajectory-based nonadiabatic dynamics with time-dependent density functional theory, Chem. Phys. Chem. **14**, 1314 (2013).

[36] S. Yamada, M. Noda, K. Nobusada, and K. Yabana, Time-dependent density functional theory for interaction of ultrashort light pulse with thin materials, Phys. Rev. B **98**, 245147 (2018).

[37] Z. X. Hu, J. Hedley, B. J. Gallacher, and I. Arce-Garcia, Dynamic characterization of MEMS using Raman spectroscopy, J. Micromech. Microeng. **18**, 095019 (2008).

[38] S. K. Ghosh and A. K. Dhara, Density-functional theory of many-electron systems subjected to time-dependent electric and magnetic fields, Phys. Rev. A **38**, 1149 (1988).

[39] G. Vignale, Mapping from current densities to vector potentials in time-dependent current density functional theory, Phys. Rev. B **70**, 201102(R) (2004).

[40] N. Troullier and J. L. Martins, Efficient pseudopotentials for plane-wave calculations, Phys. Rev. B **43**, 1993 (1991).

[41] L. Kleinman and D. Bylander, Efficacious Form for Model Pseudopotentials, Phys. Rev. Lett. **48**, 1425 (1982).

[42] G. F. Bertsch, J.-I. Iwata, A. Rubio, and K. Yabana, Real-space, real-time method for the dielectric function, Phys. Rev. B **62**, 7998 (2000).

[43] D. F. Edwards and H. R. Philipp, *Handbook of Optical Constants of Solids*, Academic Press Handbook Series Vol. 1 (Academic Press, United States, 1985), p. 665.

[44] M. Noda, S. A. Sato, Y. Hirokawa, M. Uemoto, T. Takeuchi, S. Yamada, A. Yamada, Y. Shinohara, M. Yamaguchi, K. Iida, I. Floss, T. Otobe, K.-M. Lee, K. Ishimura, T. Boku, G. F. Bertsch, K. Nobusada, and K. Yabanad, SALMON: Scalable *ab-initio* light-matter simulator for optics and nanoscience, Comput. Phys. Commun. **235**, 356 (2019).

[45] SALMON, http://salmon-tddft.jp/.

[46] Y.-X. Yan, E. B. Gamble Jr., and K. A. Nelson, Impulsive stimulated scattering: General importance in femtosecond laser pulse interactions with matter, and spectroscopic applications, J. Chem. Phys. **83**, 5391 (1985).